International Journal of Computational Methods and Experimental Measurements
Vol. 12, No. 3, September, 2024, pp. 203-215
Journal homepage: http://iieta.org/journals/ijcmem

Radiative Chemically MHD Non-Newtonian Nanofluid Flow over an Inclined Stretching Sheet with Heat Source and Multi-Slip Effects

Pennelli Saila Kumari[1], Shaik Mohammed Ibrahim[1], Prathi Vijaya Kumar[2], Giulio Lorenzini[3*]

[1] Department of Mathematics, Koneru Lakshmaiah Education Foundation, Green Fields, Vaddeswaram 522302, India
[2] Department of Mathematics, GITAM (Deemed to be University), Visakhapatnam 530045, India
[3] Department of Engineering and Architecture, University of Parma, Parma 43124, Italy

Corresponding Author Email: giulio.lorenzini@unipr.it

Copyright: ©2024 The authors. This article is published by IIETA and is licensed under the CC BY 4.0 license (http://creativecommons.org/licenses/by/4.0/).

https://doi.org/10.18280/ijcmem.120302

Received: 7 August 2024
Revised: 10 September 2024
Accepted: 19 September 2024
Available online: 30 September 2024

Keywords:
nanofluid, Casson, MHD, thermal radiation, heat source, multiple slip effects, HAM method

ABSTRACT

The present work is focused on the simulation of Casson (non-Newtonian) nanofluid flow over an inclined stretching sheet. The study considers the influence of an imposed magnetic field, heat source/sink, thermal radiation and chemical reaction under the multi slip effects. The study includes the application of wall suction/injection and Navier's first-order slip to analyse the velocity, temperature, and concentration at the wall. The governing equations have been transformed into nonlinear ordinary differential equations (ODEs) with similarity transformations. By employing the homotopy analysis method (HAM), we have successfully derived the numerical solution for the nonlinear ordinary differential equations (ODEs) and their corresponding boundary conditions. The impact of various parameters on the velocity, temperature, and concentration field has also been demonstrated. Multiple slip flow is utilised in various practical domains like micro-electro-mechanical systems, nano-electro-mechanical systems, micro-organism flow, and rarefied gas flow, among others.

1. INTRODUCTION

The unique thermal, mechanical, and chemical properties of nanofluids, a mixture of nanoparticles adjourned in a base fluid, make them perfect for enlightening lubrication, increasing thermal conductivity, and improving the performance of a variety of systems. The study of nanofluid dynamics is still in its early stages, with efforts being made to create new nanofluid formulations, increase their stability, forecast their behaviour in various scenarios, and improve their performance in a range of applications. It is true that Choi and Eastman [1] significantly advanced in the field of nanomaterials. Their research concentrated on using nanoparticles to increase a fluid's thermal conductivity. The addition of a small amount of nanoparticles in heat transfer fluids results in the new thermal phenomena of nanofluids (nanoparticle-fluid suspensions) reported by Pil Jang and Choi [2]. Meyer et al. [3] investigated computational techniques for studying fluid dynamics, while focusing on numerical approaches to nanofluid flow analysis. Akbari et al. [4] researched on the comparisons between different concepts of fluid flow likely looks at the benefits and distinctions between different models for fluid behaviour prediction. Wong and De Leon [5] engrossed in dispensing an extensive scope of present and anticipated nanofluid applications, stressing their more controllable heat allocation abilities and the unique properties that make nanofluids appropriate for such uses.

Due to of its wide-ranging applications and implications, non-Newtonian fluid flow requires careful study and modelling in the industrial and engineering sectors. Unlike Newtonian fluids like water or air, non-Newtonian fluids lacked to investigate the direct association between shear tension and shear proportion. Rather, variables such as shear rate, time, or stress can affect their viscosity. For a variety of industries, careful and precise modelling of the behaviour of non-Newtonian fluids is essential. As an illustration: Non-Newtonian fluids are frequently found in the production of paints, food products, and polymers. A wide range of food products, including dough, sauces, and creams, behave in ways that are not Newtonian. Siddappa and Abel [6] considered the study of boundary layer flow past a stretching plate in non-Newtonian like visco-elastic fluid flow. Different non-Newtonian nanofluid flows are purposefully designed by Khan [7, 8] for abundant configuration.

Because of their relationship between shear stress and strain, Casson fluids are non-Newtonian due to their sole rheological characteristics. These fluids are appropriate for shear diluting implementation because of their notable shear viscosity and yield stress. In the beginning, Casson [9] introduced the Casson fluid model for silicon dissolution and gel pens. Human blood, concentrated fruit liquids, jellies, honey, soups, and tomato sauces are a few examples of Casson fluids. In a stretching sheet, Dandapat et al. [10] examined about stability of MHD path in a viscoelastic liquid or gas, while Fang et al. [11] investigated the extended Blasius equation. Mamalouka et al. [12] discussed about the difference in solving the second order problems on a fluid that flows over an augmentation. This condition is expected to be mixed convection within the particular field when forced convection and free/natural convection cooperate to facilitate easier heat transfer. The enhanced thermal transference for miscellaneous Casson flow of nanofluid influence by external magnetism over a rotating sheet was investigated by Ali et al. [13]. Intentional aspects of the temperature and molar variation with respect to Arrhenius activation energy are discussed by Alsallami et al. [14].

Magnetohydrodynamic (MHD) flows are driven by curiosity and application: they are recycled to treat cancerous tumours, reduce bleeding from surgical wounds, distribute specific medications using magnetic particles, and detect illness using magnetic resonance imaging (MRI). The study of MHD examines the relationship between magnetic fields and fluid flow, which is a branch of mathematics. The MHD boundary layer flow above a permeable elongation area finds petition claims in the trade of crystal Fiber, paper crafting, plasma education, fuel trades, MHD control producer, boundary regulator in aero mechanics and fear of fissionable containers. Many conceptual as well as creative investigations caused some researchers to argue. Ishak [15] observed (MHD) boundary layer movement brought on by an increasing rapidly elongating sheet with radiation outcome. The viscosity factor of a magnetohydrodynamics (MHD) nanofluid is discussed by Shahid et al. [16] and is dependent on temperature. As a result of its abundant tenders in engineering complications, the influence of an outermost magnetic field on magnetohydrodynamic (MHD) deluge a lengthening area of spreading is highly notable in the field of fluid mechanics. The impact of an outward applied magnetism on Magnetohydrodynamics flow across an elongating membrane was examined by Pavlov [17]. Anderson [18] examined the viscous fluid MHD flow at the end of a stretching sheet. The distribution of heat away from the surface is largely influenced by thermal radiation. It has claims in trade industries like space exploration, missiles, atomic furnaces, planetary vehicles, choppers, satellites, and actions involving high temperatures. More grades regarding the movement of a nanofluid in the occurrence of mass as well as heat were noted in the studies [19, 20]. An elemental response has broad tenders that cover the destruction of crops by freezing, food distribution, newspaper exchange, ventilation, tile work, sunstroke protocols, and river suspensions and petroleum. Seyedi et al. [21] framework is ideal for mathematically analysing the influence of a biological response to direct heat emission on an embracing Eyring-Powell fluid channel distortion. It is feasible to implement a no-slip boundary condition when the fluid particles are near the external and are unable to transfer along with it or after the bond expires coherence. Viscous liquids prevent this marvel from happening because smooth walls sufficient, a firm surface may cause them to slip. In many situations, including wire mesh rough surfaces, greased surfaces, and covered surfaces, slip conditions become important. The change in uses characteristic of nature and modern technology has led to an important amplification in count, heat, and mass transport along with chemical reactions. Fluid flow involves chemical processes such as refrigeration fortifications, mist generation, and ceramic business. The integral transform analysis of mass and heat diffusion of chemically reacting systems with Michaelis–Menten kinetics was prepared by Pinheiro et al. [22].

The mass flow caused by a temperature gradient is indicated by the Soret result. The Soret effect has been incorporated by numerous researchers into their studies to discuss these issues and emphasize their significance. The learning of the boundary layer flow produced by an elongating sheet was primarily done by Crane [23]. He provided a precise fix for the initial issue. As time has passed by, the boundary layer flow over regular and irregular widening of surface areas has piqued the enormous interest of numerous researchers [24-27]. The reputation of mutable nanomaterial radius for the non-Newtonian flow of nanofluid promoted through a stretching sheet is discussed by Ali et al. [28]. An elastic limit that is similar to the constant harvest tension in Casson fluid occurs, if the rouleaux entertains similar an elastic solid studied by Fung [29]. The ideal point flow and heat allocation in a Casson fluid flow ended an elongating plate are discussed by Mustafa et al. [30]. Shehzad et al. [31] supplied a thoughtful answer to the stable boundaryed layer flow of a Casson fluid above an absorbent elongating plate. Investigators have been captivated by the potential of exponentially stretching cylinders in a variety of domains, such as polymer dispensation, purification, biomedical tenders, and energy change systems. An investigation into the analogous determination of the flow features and transmission of heat inside a constant Casson-based nanofluid stirring diagonally crosswise erectly situated cylinder exposed to spreading radial extension was guided by Naseer et al. [32]. Merkin et al. [33] observed the thermal features of the boundaryed sheet flow at a recession fact connecting a volumetric curve that causes exponentially stretched sheet. Malik et al. [34] investigated cautiously the comparable conclusions regarding the flow properties and heat exchange of a stable Casson-based nanofluid applied inclined to a vertically positioned cylinder subjected to exponential radial stretching sheet. The combination of a magnetic field and a heat source affects on Casson nanofluid flow in a stable boundary layer, as done by Sarojamma and Vendabai [35]. In measuring thermophoretic diffusion properties and Brownian motion, Mustafa et al. [36] examined the merged convective move of magneto-nanofluid that was controlled by vertical stretched plate. Awais et al. [37] measured the outcomes of heat source/sink and mass and heat transfer on Casson fluid flow through a vertically exponentially stretched/shrinking sheet using mathematical analysis. Zhai et al. [38] have derived the relation between the mass transfer and heat structures for a variety of disorders and absorbers. Thermal and stratification characteristics of non-Newtonian fluid passes through a porous medium was investigated by Megahed and Abbas [39]. Through the use of FDM, Barik et al. [40] examined the impact of multiple slips effects on the flow of MHD nanofluids over an inclined, radiative, and chemically reactive stretched sheet.

We found that a very few studies have investigated the thermo-hydro-dynamics properties of Casson and nanofluid over an inclined stretching sheet by taking into account all the different phenomena, including variables like magnetic field, linear radiation, an external heat source/sink, and the chemical reaction, from the aforementioned literature survey. It is anticipated that slip exists at the surface in this investigation because nanofluid has been used as the working fluid. To analyze these phenomena, the research employs established similarity variables, converting the primary partial differential equations (PDEs) into a set of interconnected ordinary differential equations (ODEs). These ODEs are numerically resolved by using employing the homotopy analysis method (HAM), This methodology ensures the generation of robust data across various parameters. To validate the computed results, a comparative analysis is performed against existing research data. The research makes a significant contribution to our understanding of non-Newtonian nanofluid flow by elucidating the complex interactions among various elements that govern micro rotational transport in a non-Newtonian nanofluid, as characterized by the Casson nanofluid model.

2. MATHEMATICAL FORMULATION

In the present study, a steady, two-dimensional, incompressible, laminar flow of nanofluid over a stretching sheet which is inclined at an angle *Ω* from its vertical axis. The x- and y- axes are aligned along the inclined surface and normal to the surface as depicted in Figure 1. Stretching has been accomplished by moving the wall with a velocity $U_w=ax$, $a>0$ along the x-axis. The MHD, thermal, as well as the concentration boundary layers are supposed to develop along the *y*- axis, and grow along the *x*-axis. The velocity, temperature, and concentration of the nanofluid on the wall are *Uw*, *Tw*, and *Cw*, respectively. The velocity, temperature, and the concentration fields are taken as $U_\infty=bx$, T_∞ and C_∞ as as $y\to\infty$. It is assumed that thermal equilibrium prevailed between the nanoparticles and base fluid with having slip between them. A uniform magnetic field of strength B_0 has been applied normal to the x-axis, and over the entire fluid domain. In the present study, the effects of the thermal radiation, chemical reaction, and the buoyancy on the velocity, temperature, and concentration profiles in the presence of the multiple slip conditions at the wall are considered under suction/injection. External heat source/sink is also considered in the energy equation. The body force terms due to the thermal and concentration gradients are included in the momentum equation. The properties of Brownian motion and thermophoresis are considered.

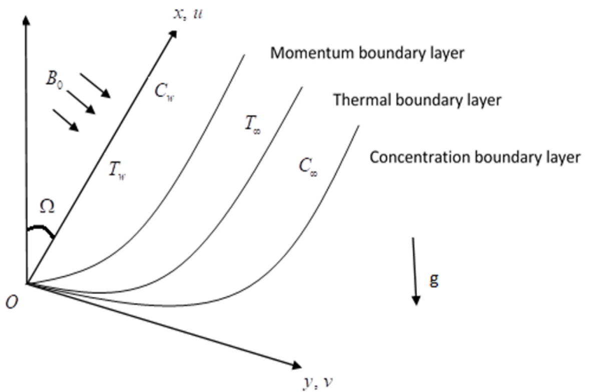

Figure 1. Physical model of the flow

The visco-elastic equation of state for an isotropic and flexible flow of Casson fluid is:

$$\tau_{ij} = \begin{bmatrix} 2\left(\mu_B + \dfrac{p_y}{\sqrt{2\pi}}\right)e_{ij}, & \pi > \pi_c \\ 2\left(\mu_B + \dfrac{p_y}{\sqrt{2\pi_c}}\right)e_{ij}, & \pi_c > \pi \end{bmatrix}$$

where, μ_B is plastic dynamic viscosity of the non-Newtonian fluid, p_y is the yield stress of the fluid, π is the product of the constituent of deformation rate with itself, e_{ij} is the (i,j)th component of the deformation rate and π_c is the vital tone of this product based on the non-Newtonian model. For the case of Casson fluid, we measured $\pi>\pi_c$ and $p_y = \frac{\mu_B\sqrt{2\pi}}{\beta}$, it is probable to say that the dynamic viscosity $\mu = \mu_B + \frac{p_y}{\sqrt{2\pi}}$.

Substituting the value of p_y in μ, we get $\mu = \mu_B\left(1+\frac{1}{\beta}\right)$.

In the perspective of the boundary layer approximation, the governing differential equations for continuity, momentum, energy, and the nanofluid concentration are written as follows [40]:

$$\frac{\partial u}{\partial x} + \frac{\partial v}{\partial y} = 0 \tag{1}$$

$$\begin{aligned} &u\frac{\partial u}{\partial x} + v\frac{\partial u}{\partial y} = \upsilon\left(1+\frac{1}{\beta}\right)\frac{\partial^2 u}{\partial y^2} \\ &+g\left[\beta_T\left(T-T_\infty\right)+\beta_C\left(C-C_\infty\right)\right]\cos\Omega \\ &+U_\infty\frac{dU_\infty}{dx} + \frac{\sigma_f B^2(x)}{\rho_f}\left(U_\infty - u\right) \end{aligned} \tag{2}$$

$$\begin{aligned} &u\frac{\partial T}{\partial x} + v\frac{\partial T}{\partial y} = \alpha\frac{\partial^2 T}{\partial y^2} \\ &+\tau\left[D_B\frac{\partial C}{\partial y}\frac{\partial T}{\partial y} + \frac{D_T}{T_\infty}\left(\frac{\partial T}{\partial y}\right)^2\right] \\ &+\frac{Q_0}{(\rho c)_f}\left(T-T_\infty\right) - \frac{1}{(\rho c)_f}\frac{\partial q_r}{\partial y} \end{aligned} \tag{3}$$

$$u\frac{\partial C}{\partial x} + v\frac{\partial C}{\partial y} = D_B\frac{\partial^2 C}{\partial y^2} + \frac{D_T}{T_\infty}\frac{\partial^2 T}{\partial y^2} - Kr\left(C-C_\infty\right). \tag{4}$$

Succeeding Barik et al. [40], the boundary conditions are considered as:

$$\begin{aligned} &u = U_w(x) + \delta_1^*\left(\frac{\partial u}{\partial y}\right), \\ &v = V_w,\ \ T = T_w(x) + \delta_2^*\left(\frac{\partial T}{\partial y}\right), \\ &C = C_w(x) + \delta_3^*\left(\frac{\partial C}{\partial y}\right) \ \text{ at } \ y=0 \\ &u\to U_\infty, \quad T\to T_\infty, \ \ C\to C_\infty, \ \text{as} \quad y\to\infty \end{aligned} \tag{5}$$

where, $\alpha = \frac{k}{(\rho c)_f}$, $\upsilon = \frac{\mu}{\rho_f}$, $\tau = \frac{(\rho c)_p}{(\rho c)_f}$.

Succeeding Roseland approximation, the radiative heat flux is:

$$q_r = -\frac{4\sigma^*}{3\kappa^*}\frac{\partial T^4}{\partial y} \tag{6}$$

where, Stefan Boltzmann constant is σ^* and κ^* is the mean absorption coefficient. Furthermore, we assume that the flow's interior temperature differential is sufficiently vast so that T^4 is denoted as a linear function of temperature. As a solution, by enlarging T^4 in Taylor series about T_∞ and if we disregard terms of higher order, we get:

$$T^4 \cong 4T_\infty^3 T - 3T_\infty^4, \tag{7}$$

Using Eqs. (6) and (7), Eq. (3) converts into:

$$u\frac{\partial T}{\partial x}+v\frac{\partial T}{\partial y} = \left(\alpha+\frac{16\sigma^* T_\infty^3}{3\kappa^*(\rho c)_f}\right)\frac{\partial^2 T}{\partial y^2}+\tau\left[D_B\frac{\partial C}{\partial y}\frac{\partial T}{\partial y}+\frac{D_T}{T_\infty}\left(\frac{\partial T}{\partial y}\right)^2\right]+\frac{Q_0}{(\rho c)_f}(T-T_\infty), \tag{8}$$

Using following similarity transformations:

$$\psi=(av)^{\frac{1}{2}}xf(\zeta),\theta(\zeta)=\frac{T-T_\infty}{T_W-T_\infty}, \quad \phi(\zeta)=\frac{C-C_\infty}{C_W-C_\infty}, \zeta=\sqrt{\frac{a}{v}}y \tag{9}$$

where, ζ is the similarity variable, ψ is the stream function.

The stream function ψ is formalized in the standard way as:

$$u=\frac{\partial\psi}{\partial y}, \qquad v=-\frac{\partial\psi}{\partial x} \tag{10}$$

substituting Eq. (9) in Eqs. (2), (4) and (8), we obtain:

$$\left(1+\frac{1}{\beta}\right)f'''+ff''-f'^2 +(Gr\theta+Gc\phi)\cos\Omega+M(A-f')+A^2=0, \tag{11}$$

$$\left(1+\frac{4}{3}R\right)\theta''+\Pr f\theta' +\Pr Nb\phi'\theta'+\Pr Nt\,\theta'^2+\Pr Q\theta=0, \tag{12}$$

$$\phi''+Sc(f\phi'-\gamma\phi)+\frac{Nt}{Nb}\theta''=0. \tag{13}$$

The boundary conditions are:

$$f(0)=S,\ f'(0)=1+\left(1+\frac{1}{\beta}\right)\delta_1 f''(0), \quad \theta(0)=(1+\delta_2\theta'(0)),\ \phi(0)=(1+\delta_3\phi'(0)), \quad f'(\infty)\to A,\theta(\infty)\to 0,\phi(\infty)\to 0 \tag{14}$$

where,
$\beta=\frac{\mu_B\sqrt{2\pi_C}}{p_y}$, $M=\frac{\sigma_f B_0^2}{\rho_f a}$, $Gr_x=\frac{g\beta_T(T_W-T_\infty)x^3}{v^2}$, $Gr=\frac{Gr_x}{Re_x^2}$, $Gc_x=\frac{g\beta_C(C_W-C_\infty)x^3}{v^2}$, $Gc=\frac{Gc_x}{Re_x^2}$, $Re_x=\frac{U_W x}{v}=\frac{ax^2}{v}$, $A=\frac{b}{a}$, $Pr=\frac{v}{\alpha}$, $Nb=\frac{\tau D_B(C_W-C_\infty)}{v}$, $Nt=\frac{\tau D_T(T_W-T_\infty)}{vT_\infty}$, $R=\frac{4\sigma^* T_\infty^3}{k^* k}$, $Q=\frac{Q_0}{a(\rho c)_f}$, $Sc=\frac{v}{D_B}$, $\gamma=\frac{Kr}{a}$, $\delta_1=\delta_1^*\sqrt{\frac{a}{v}}$, $\delta_2=\delta_2^*\sqrt{\frac{a}{v}}$, $\delta_3=\delta_3^*\sqrt{\frac{a}{v}}$, $S=-\frac{V_W}{\sqrt{av}}$.

2.1 HAM

To express the homotopic results of Eqs. (11) to (14), we gross up the primary deductions and linear operators as follows:

$$f_0(\zeta)=S+A\zeta+\left(\frac{1-A}{1+\delta_1\left(1+\frac{1}{\beta}\right)}\right)(1-e^{-\zeta}),$$
$$\theta_0(\zeta)=\frac{e^{-\zeta}}{1+\delta_2},\ \phi_0(\zeta)=\frac{e^{-\zeta}}{1+\delta_3},$$
$$L_f(f)=f'''-f',\ L_\theta(\theta)=\theta''-\theta,\ L_\phi(\phi)=\phi''-\phi,$$
with $L_f(D_1+D_2e^{\zeta}+D_3e^{-\zeta})=0$, $L_\theta(D_4e^{\zeta}+D_5e^{-\zeta})=0$, $L_\phi(D_6e^{\zeta}+D_7e^{-\zeta})=0$,

where, D_i (i=1 to 7) are the arbitrary constants.

We construct the zeroth-order deformation equations:

$$(1-p)L_f\left(f(\zeta;p)-f_0(\zeta)\right) = p\hbar_f N_f\left[f(\zeta;p),\theta(\zeta;p),\phi(\zeta;p)\right], \tag{15}$$

$$(1-p)L_2\left(\theta(\zeta;p)-\theta_0(\zeta)\right) = p\hbar_\theta N_\theta\left[f(\zeta;p),\theta(\zeta;p),\phi(\zeta;p)\right], \tag{16}$$

$$(1-p)L_\phi\left(\phi(\zeta;p)-\phi_0(\zeta)\right) = p\hbar_\phi N_\phi\left[f(\zeta;p),\theta(\zeta;p),\phi(\zeta;p)\right], \tag{17}$$

subject to the boundary conditions:

$$f(0;p)=S,\ f'(0;p)=\left[1+\delta_1\left(1+\frac{1}{\beta}\right)f''(0)\right], \quad f'(\infty;p)=0, \quad \theta(0;p)=\left[1+\delta_2\theta'(0)\right],\ \ \theta(\infty;p)=0, \quad \phi(0;p)=\left[1+\delta_3\phi'(0)\right],\ \ \phi(\infty;p)=0, \tag{18}$$

where,

$$N_f\left[f(\zeta;p),\theta(\zeta;p),\phi(\zeta;p)\right] =\left(1+\frac{1}{\beta}\right)\delta\frac{\partial^3 f(\zeta;p)}{\partial\zeta^3}+f(\zeta;p)\frac{\partial^2 f(\zeta;p)}{\partial\zeta^2} -\left(\frac{\partial f(\zeta;p)}{\partial\zeta}\right)^2+A^2+M\left(A-\frac{\partial f(\zeta;p)}{\partial\zeta}\right) +\left(Gr\,\theta(\zeta;p)+Gc\,\phi(\zeta;p)\right)\cos\Omega, \tag{19}$$

$$N_\theta\left[f(\zeta;p),\theta(\zeta;p),\phi(\zeta;p)\right] =\frac{1}{\Pr}\left(1+\frac{4}{3}R\right)\frac{\partial^2\theta(\zeta;p)}{\partial\zeta^2} +f(\zeta;p)\frac{\partial\theta(\zeta;p)}{\partial\zeta}+Nb\frac{\partial\theta(\zeta;p)}{\partial\zeta}\frac{\partial\phi(\zeta;p)}{\partial\zeta} +Nt\left(\frac{\partial\theta(\zeta;p)}{\partial\zeta}\right)^2+Q\theta(\zeta;p), \tag{20}$$

$$N_{\phi}\left[f(\zeta;p),\theta(\zeta;p),\phi(\zeta;p)\right] = \frac{\partial^2\phi(\zeta;p)}{\partial\zeta^2} + Sc\, f(\zeta;p)\frac{\partial\phi(\zeta;p)}{\partial\zeta} + \frac{Nt}{Nb}\frac{\partial^2\theta(\zeta;p)}{\partial\zeta^2} - Sc\,\gamma\phi(\zeta;p), \tag{21}$$

where, $p \in [0,1]$ is the embedding parameter, $\hbar_f, \hbar_\theta$ and $\hbar_\phi$ are non-zero auxiliary parameters and N_f, N_θ and N_ϕ are nonlinear operators.

The nth-order deformation equations are follows:

$$L_f\left(f_n(\zeta) - \chi_n f_{n-1}(\zeta)\right) = \hbar_f R_n^f(\zeta), \tag{22}$$

$$L_\theta\left(\theta_n(\zeta) - \chi_n \theta_{n-1}(\zeta)\right) = \hbar_\theta R_n^\theta(\zeta), \tag{23}$$

$$L_\phi\left(\phi_n(\zeta) - \chi_n \phi_{n-1}(\zeta)\right) = \hbar_\phi R_n^\phi(\zeta), \tag{24}$$

with the following boundary conditions:

$$f_n(0)=0,\ f_n'(0)=\delta_1\left(1+\frac{1}{\beta}\right)f_n''(0),\ f_n'(\infty)\to 0, \quad \theta_n(0)=\delta_2\theta_n'(0),\ \theta_n(\infty)\to 0;\ \phi_n(0)=\delta_3\phi_n'(0),\ \phi_n(\infty)\to 0 \tag{25}$$

where,

$$R_n^f(\zeta) = \left(1+\frac{1}{\beta}\right)f_{n-1}''' + \sum_{i=0}^{n-1} f_{n-1-i} f_i'' - \sum_{i=0}^{n-1} f_{n-1-i}' f_i' + (1-\chi_n)(A^2+M) - M f_{n-1}' + (Gr\,\theta_{m-1} + Gc\,\phi_{m-1})\cos\Omega, \tag{26}$$

$$R_n^\theta(\zeta) = \frac{1}{\Pr}\left(1+\frac{4R}{3}\right)\theta_{n-1}'' + \sum_{i=0}^{n-1} f_{n-1-i}\theta_i' + Nb\sum_{i=0}^{n-1}\theta'_{n-1-i}\phi_i' + Nt\sum_{i=0}^{n-1}\theta'_{n-1-i}\theta_i' - \Pr Q\,\theta_{n-1}, \tag{27}$$

$$R_n^\phi(\zeta) = \phi_{n-1}'' + Sc\left(\sum_{i=0}^{n-1} f_{n-1-i}\phi_i' - \gamma\phi_{n-1}\right) + \frac{Nt}{Nb}\theta_{n-1}'', \quad \chi_n = \begin{cases} 0, & n \le 1, \\ 1, & n > 1. \end{cases} \tag{28}$$

If we let $f_n^*(\zeta), \theta_n^*(\zeta)$ and $\phi_n(\zeta)$ as the different results of m[th] order deformation equations, then the general solution is given by:

$$f_n(\zeta) = f_n^*(\zeta) + D_1 + D_2 e^{\zeta} + D_3 e^{-\zeta}, \quad \theta_n(\zeta) = \theta_n^*(\zeta) + D_4 e^{\zeta} + D_5 e^{-\zeta}, \quad \phi_n(\zeta) = \phi_n^*(\zeta) + D_6 e^{\zeta} + D_7 e^{-\zeta} \tag{29}$$

where, the integral constants D_i (i=1 to 7) using the boundary conditions.

It is effortless to solve the above linear homogeneous equations using MATHEMATICA one after other in the order n=1, 2, ….

2.2 Convergence of HAM

To obtain the appropriate values for the non-zero auxiliary parameters, $\hbar$ -curves are depicted in Figure 2. From this figure, the auxiliary parameter is given by the supposable interval [-1.0,0.0]. The solutions are convergent for whole region of ζ when $\hbar_f = \hbar_\theta = \hbar_\phi = -0.72$. Convergence of the method is given in Table 1.

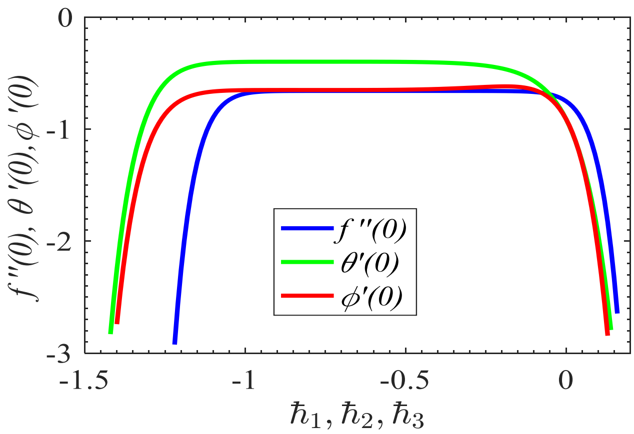

Figure 2. $\hbar$ -curves for $f''(0)$, $\theta'(0)$ and $\varphi'(0)$ at 15[th] order approximations

3. RESULTS AND DISCUSSIONS

The association between different factors and their consequences on f', θ and ϕ of the fluid flow is explored in detail in this section. Additionally, we elucidate the parameters associations between these profiles and important dimensionless variables, such as the skin friction coefficient, the local Nusselt number and the local Sherwood number. In order to shed light on these connections, we employ a set of informative graphs. As a way to preserve coherence with the numerical results generated in this study, we strictly follow the predetermined values shown in Table 1, unless there are specific deviations indicated in the relevant figures.

Table 1. Convergence of HAM solution for different orders of approximations when β=1.0, M=0.5, Ω=60°, $S=R=A=\delta_1=\delta_2=\delta_3=Q=Gr=Gc$=0.1, $Pr=Sc$=1.0, Nb=0.3, Nt=0.2, γ=0.2

Order	$-f''(0)$	$-\theta'(0)$	$-\phi''(0)$
5	-1.316344	0.463692	0.633936
10	-1.317255	0.450865	0.650285
15	-1.317248	0.451028	0.650438
20	-1.317248	0.451025	0.650431
25	-1.317248	0.451024	0.650432
30	-1.317248	0.451024	0.650432
35	-1.317248	0.451024	0.650432
40	-1.317248	0.451024	0.650432

Figures 3-5 presented the effects of the Casson fluid parameter β on the velocity, temperature and concentration profiles. It is observed that amplification in β enhances the viscosity of the fluid. Fluid behaves like shear-thickening on behalf of an incremental change in β which lessens the fluidity of the fluid and also its wideness of the momentum boundary layer. The velocity, temperature profiles decrease with the increase of Casson fluid parameter, whereas the reverse trend is observed in concentration profile.

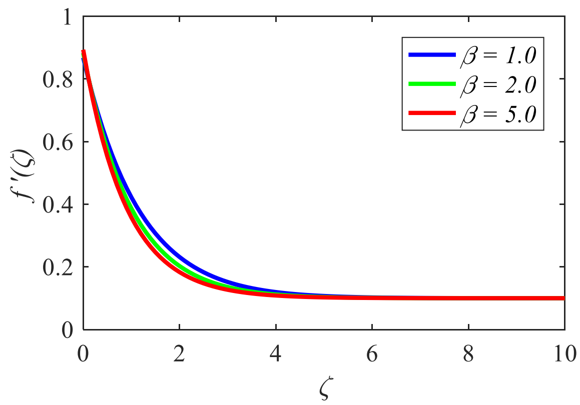

Figure 3. Figuration of $f'(\zeta)$ for β

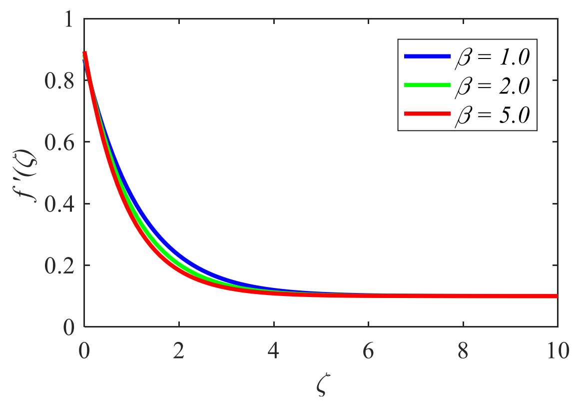

Figure 4. Figuration of $\theta(\zeta)$ for β

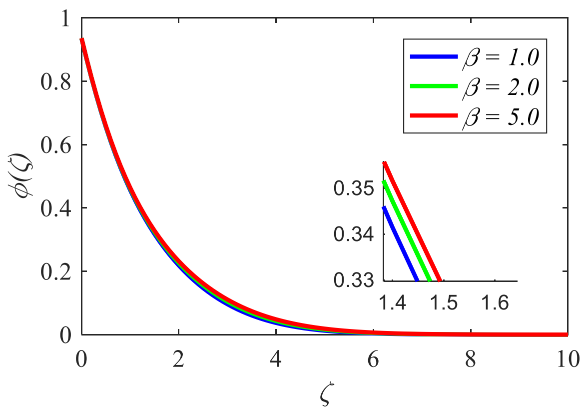

Figure 5. Figuration of $\phi(\zeta)$ for β

The influence of magnetic parameter M on the profiles is revealed in Figures 6-8. $f'(\zeta)$ decreases as M's magnitude increases, despite the opposite pattern for concentration and temperature. In actuality, as M increases, the Lorentz force which limits fluid motion increases, which causes the rate of transport to decrease. When the magnetic field was applied over the flow field, the Lorentz force became apparent. This force is strong enough to slow down the fluid's flow and drag it along. As a result, fluid flow velocity decreases as momentum layer thickness increases.

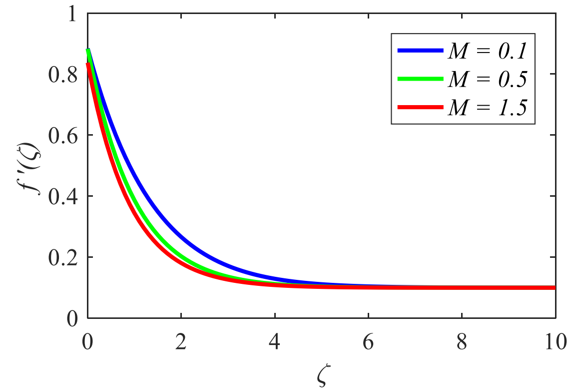

Figure 6. Figuration of $f'(\zeta)$ for M

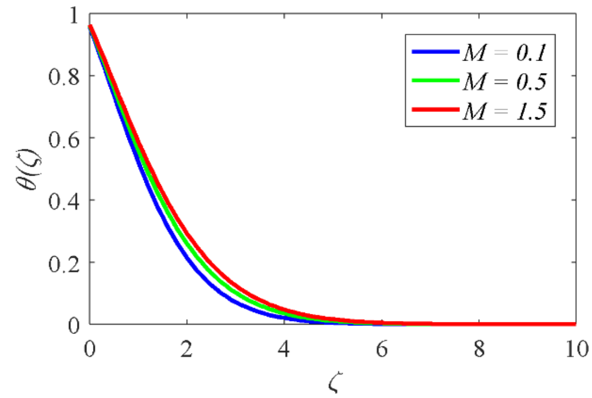

Figure 7. Figuration of $\theta(\zeta)$ for M

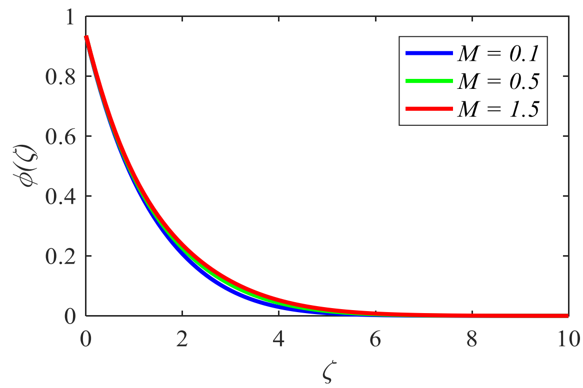

Figure 8. Figuration of $\phi(\zeta)$ for M

The influence of velocity ratio parameter A on the profiles momentum is revealed in Figure 9. The momentum of the fluid increases as velocity ratio parameter A magnitude increases. The effect of velocity ratio parameter A on the evolution of non-dimensional temperature and solutal concentration profiles is shown in Figures 10 and 11. Thin thermal and solutal boundary layers form when A values increase because the temperature and fluid concentration decrease asymptotically. An increased amount of heat transfer from the wall to the free stream is encouraged by a higher velocity ratio parameter, which also increases the free stream velocity. Because the free stream velocity increases with increasing velocity ratio parameter A, the fluid concentration likewise decreases.

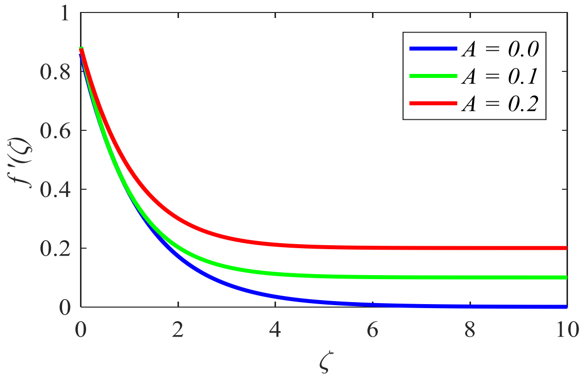

Figure 9. Figuration of $f'(\zeta)$ for A

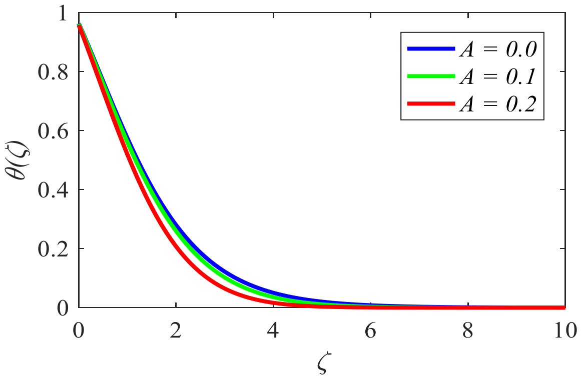

Figure 10. Figuration of $\theta(\zeta)$ for A

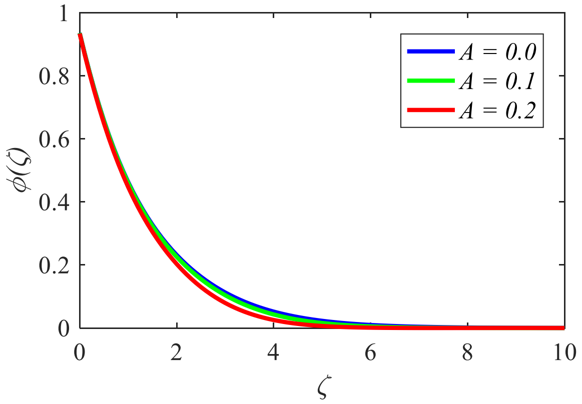

Figure 11. Figuration of $\phi(\zeta)$ for A

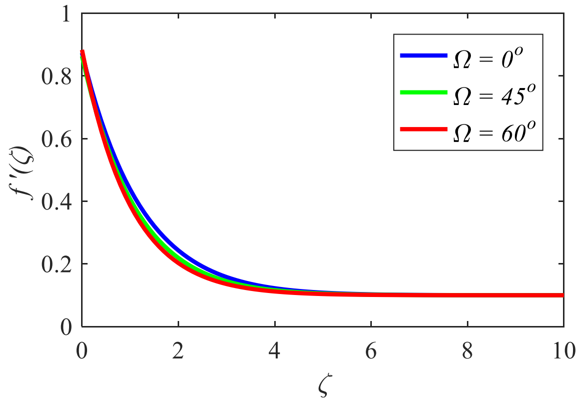

Figure 12. Figuration of $f'(\zeta)$ for Ω

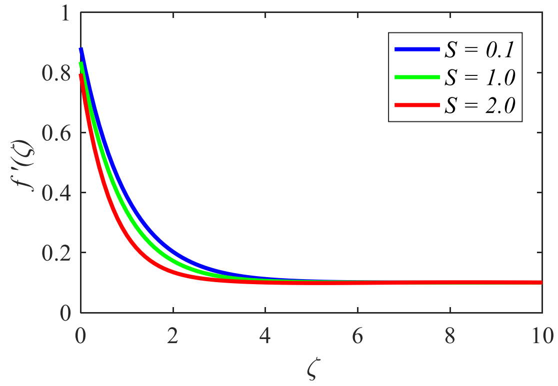

Figure 13. Figuration of $f'(\zeta)$ for S

Figure 12 demonstrates the decreasing performance of velocity for increased parameter values, specifically angle of inclination Ω. The fluid flow becomes difficult due to Lorentz forces, which lowers the fluid's velocity. The findings in Figure 13 show that increasing suction (S) efficiently lowers the velocity profile in both the gaseous and liquid states.

Figure 14 illustrates the properties of the local Grashof number *Gr* on the velocity profiles. Here, as *Gr* values rises, then the momentum of the fluid flow going to be enhanced rapidly. The velocity profiles enhance as the values of modified Grashof parameter *Gc* rises, as seen in Figure 15.

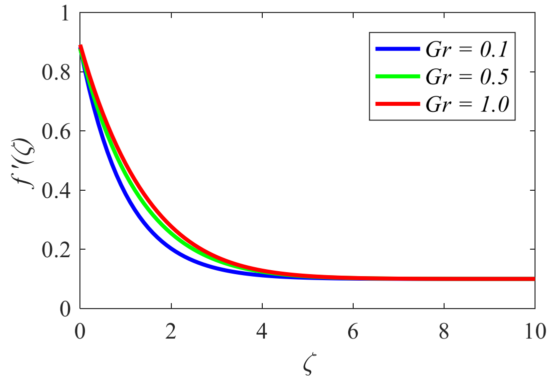

Figure 14. Figuration of $f'(\zeta)$ for *Gr*

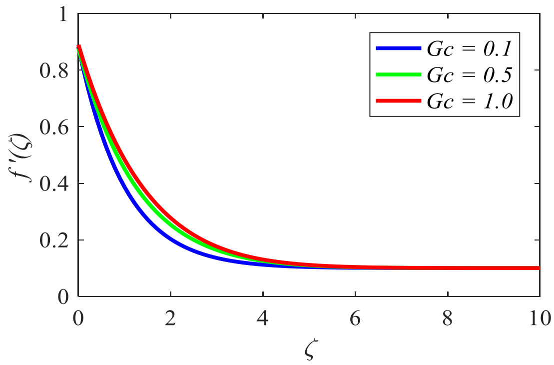

Figure 15. Figuration of $f'(\zeta)$ for *Gc*

The fluid velocity decreases, and the slip velocity rises as the velocity slip constraint δ_1 growths. This may be the case because, in the event of a slip condition, the stretching sheet's velocity and the stream's velocity differ. This is depicted in Figure 16. The fluid velocity decreases as the slip velocity increases in response to an increase in the velocity slip constraint δ_1. This phenomenon happens because the stretching sheet's velocity and the fluid stream's velocity near the sheet are dissimilar under slip conditions.

Figure 17 shows that the temperature drops as the thermal slip constraint δ_2 increases. As the thermal slip constraint value rises, the thermal boundary layer's physical width declines even though there is very little heat transfer from the sheet to the fluid. As seen in Figure 18, the influence of the nanoparticle fraction slip constraint δ_3 on the mass fraction field closely parallels that of δ_3 on the temperature field. This similarity stems from the basic impediment to liquid motion caused by slip, which eventually leads to a reduction in net atomic advancement. Consequently, the mass fraction field decreases as a result of decreased molecular development.

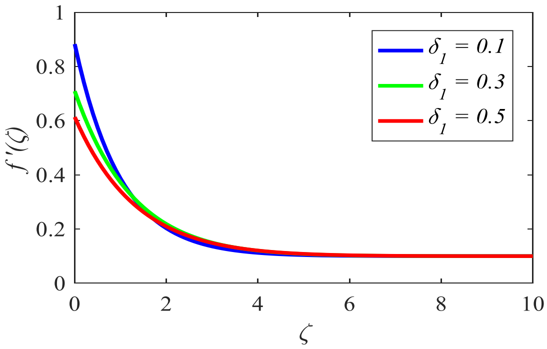

Figure 16. Figuration of $f'(\zeta)$ for δ_1

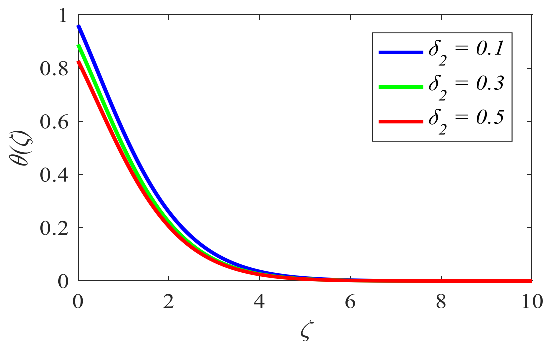

Figure 17. Figuration of $\theta(\zeta)$ for δ_2

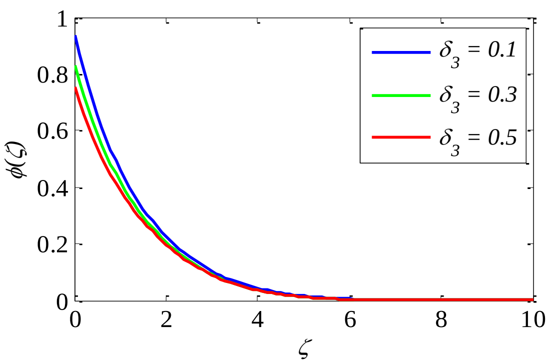

Figure 18. Figuration of $\phi(\zeta)$ for δ_3

The connection between temperature and the radiation constraint R is shown in Figure 19. Increased radiative heat energy injection into the system, which increases the temperature, is indicated by higher values of R. Figure 20 shows temperature distributions for a range of Prandtl number Pr values, showing a decline in the temperature profile with increasing Pr. Physically, smaller temperature profiles are produced by increasing Prandtl numbers. Figure 21 illustrates the remarkable impact of Q on $\theta(\zeta)$. In the instance of air, an increase in the values improves θ. After declining at first, the temperature profile rises away from the wall.

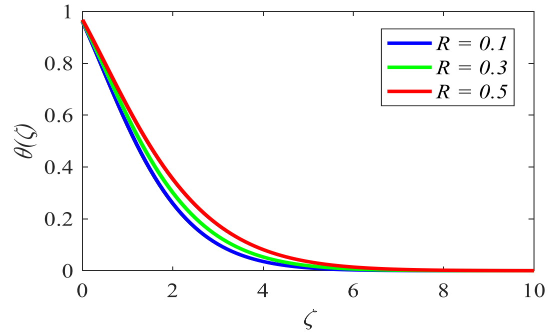

Figure 19. Figuration of $\theta(\zeta)$ for R

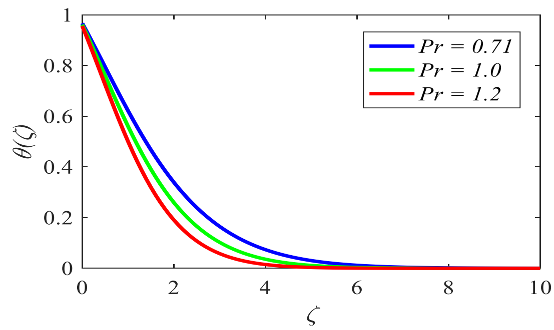

Figure 20. Figuration of $\theta(\zeta)$ for Pr

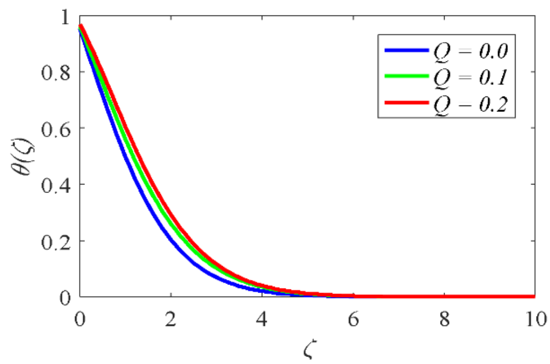

Figure 21. Figuration of $\theta(\zeta)$ for Q

Figures 22 and 23 demonstrate the significance of the Brownian movement parameter Nb affects $\theta(\zeta)$ and $\phi(\zeta)$. Generally speaking, Brownian movement aids in heating the fluid in the boundary layer and stops particles from depositing on the surface away from the fluid. The temperature rises and the concentration decreases as the amount of Nb in the fluid increases (less than 1). Usually, Brownian motion prevents molecules from depositing away from the liquid surface and heats the liquid inside the boundary layer. Rapid flow at a distance from the extension surface is caused by the thermophoretic force created by the resulting temperature gradient. As a result, as Nb rises, additional fluid is heated away from the surface, raising the temperature of the boundary layer.

Nanoparticles are transported by the fast flow created by the stretching sheet, increasing the width of the boundary layer for mass volume fraction. Figures 24 and 25 provide illustrations of these phenomena. According to reports, the temperature and the concentration of nanoparticles both increase in direct proportion to *Nt*.

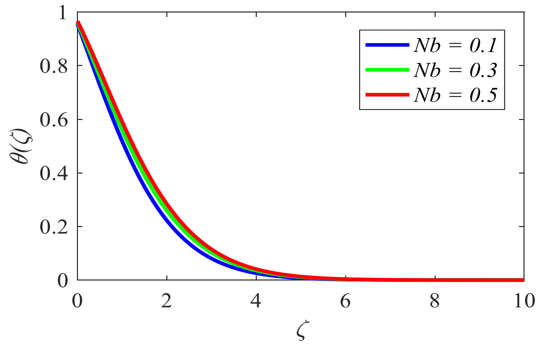

Figure 22. Figuration of $\theta(\zeta)$ or *Nb*

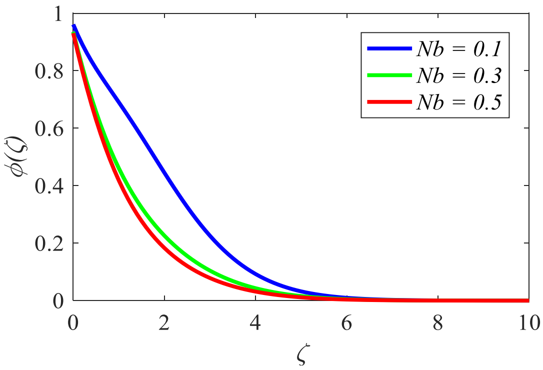

Figure 23. Figuration of $\phi(\zeta)$ or *Nb*

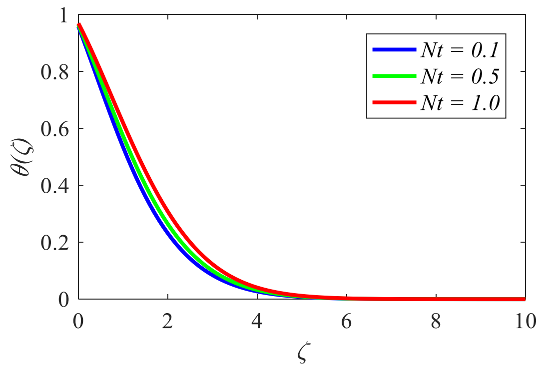

Figure 24. Figuration of $\theta(\zeta)$ for *Nt*

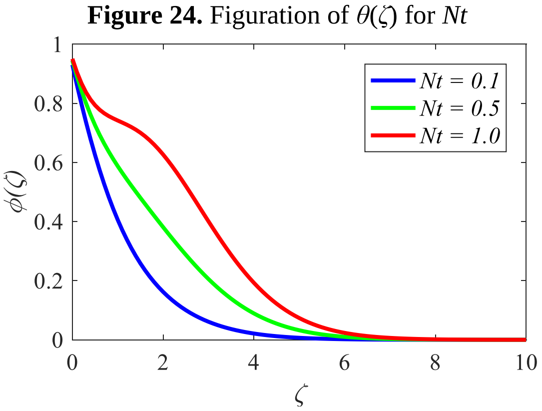

Figure 25. Figuration of $\phi(\zeta)$ for *Nt*

The influence of Schmidt number (*Sc*) on the concentration profile of $\phi(\zeta)$ is depicted in Figure 26. It has also been observed that the concentration profile decreases as the value increases. In terms of physics, *Sc* is the ratio of mass diffusivity to momentum diffusivity; an increase in the Schmidt number indicates a decrease in the fluid's mass diffusivity relative to its momentum diffusivity, which implies a decrease in scalar diffusivity and less diffusion and slower concentration changes in the fluid medium.

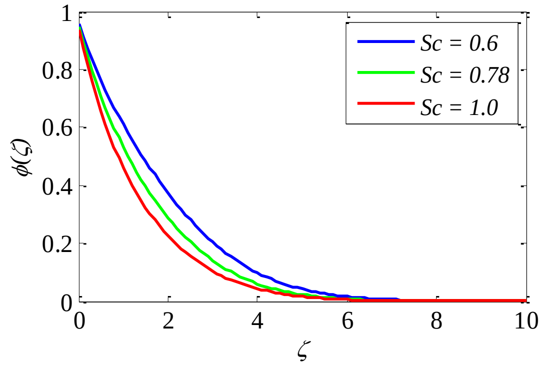

Figure 26. Figuration of $\phi(\zeta)$ for *Sc*

Figure 27 illustrates the impact of a chemical reaction parameter γ on $\phi(\zeta)$. It is known that the concentration decreases as the chemical reaction parameter increases.

Figure 28 displays the skin-friction factor on variation of *M* and δ_1. It's observed that as M and δ_1 increased the skin-friction coefficient increases.

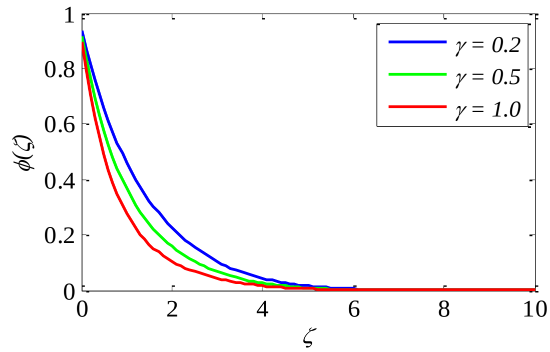

Figure 27. Figuration of $\phi(\zeta)$ for γ

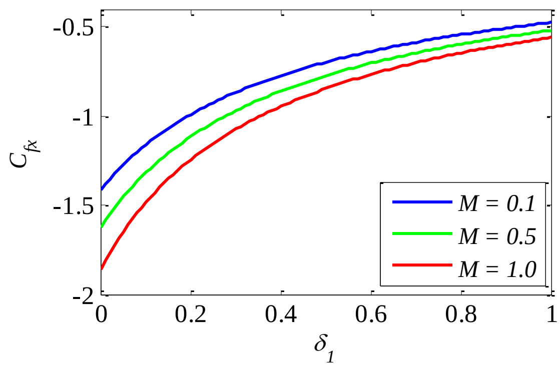

Figure 28. Figuration of C_{fx} for *M* and δ_1

In Figure 29 it is noted that Nusselt number decreases for increase both the constraints Nt and δ_2. Sherwood Number is shown in Figure 30, rise as a result of the fluid's high molecular diffusivity and low heat conductivity. The Nt and δ_3 variations are displayed. In the boundary layer, the fluid velocity near the wall decreases as Nt and δ_3 increases.

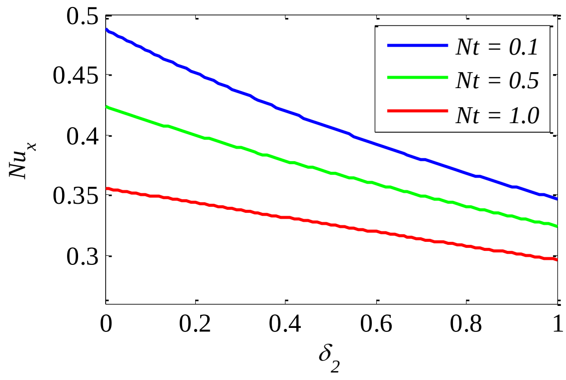

Figure 29. Figuration of Nu_x for Nt and δ_2

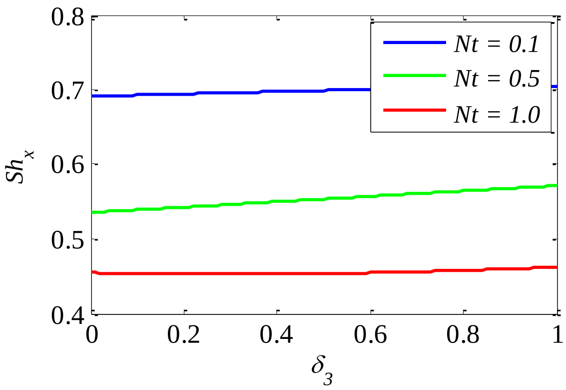

Figure 30. Figuration of Sh_x for Nt and δ_3

Table 2. Comparison of skin friction coefficient for different values of β and A when M=0, δ_1=0.0, S=0.0

β	A	Oyelakin et al. [41]	HAM
1	0.0	-1.41421	-1.41421
5	0.0	-1.09544	-1.09545
1000	0.01	-0.99782	-0.99801
1000	0.1	-0.96937	-0.96937
1000	0.2	-0.91811	-0.91811

Table 3. Comparison of $-f''(0)$ for different values of δ_1 when M=0, A=0.0, β=1000, S=0.0

δ_1	Ibrahim and Makinde [42]	Oyelakin et al. [41]	HAM
0.0	1.0000	1.000000	1.00000
0.1	0.8721	0.872083	0.87208
0.2	0.7764	0.776377	0.77638
0.5	0.5912	0.591195	0.59121
1.0	--	0.430160	0.43017
2.0	0.2840	0.283979	0.28397
3.0	--	0.214054	0.21406
5.0	0.1448	0.144714	0.14484
10.0	0.0812	0.080932	0.08125

Table 4. Evaluation of the numerical values of $-\theta'(0)$ for different values of Pr when Le=10 and in the nonappearance of remaining parameters

Pr	Rudraswamy et al. [43]	Gupta et al. [44]	Mini et al. [45]	HAM
0.2	0.1691	0.1691382	0.169124	0.169118
0.7	0.4539	0.4538682	0.453917	0.453853
2.0	0.9112	0.9113432	0.911358	0.911341

To assess the validity and accuracy of the applied numerical scheme, numerical values for skin-friction factor, the heat transfer and mass transfer coefficient for various values parameters and in the absence of different parameters are compared with the available results and the outcome is shown in Tables 2-4. The results are found in excellent agreement.

4. CONCLUSIONS

Based on numerical studies conducted using a HAM technique, the following results were drawn regarding the MHD properties of a Casson nanofluid flowing over an inclined stretching sheet that was stretched linearly:

(i) The decrease in nanofluid velocity is proportional to the Casson parameter, the magnetic parameter and velocity slip factor. The thermal radiation parameter, the Brownian motion, the heat source parameter, and all contribute to an increase in the nanofluid's temperature.

(ii) The solution boundary layer grows as the Casson parameter, thermophoresis parameter does, but it shrinks as Nb shrinks.

(iii) There is a correlation between the velocity slip parameter and an increase in the heat and mass transfer rates. However, the rate of heat transfer and the rate of mass transfer both decrease as the temperature jump parameter values increase.

(iv) It has been observed that the Nusselt number and the Sherwood number drop when the magnetic parameter increases. Through the process of velocity slip, both the Nusselt number and the Sherwood number fall.

Future scope: It is possible that the current work could be expanded to include the non-Newtonian flow over a nonlinear stretching sheet in our subsequent research activities.

REFERENCES

[1] Choi, S.U., Eastman, J.A. (1995). Enhancing thermal conductivity of fluids with nanoparticles (No. ANL/MSD/CP-84938; CONF-951135-29). Argonne National Lab. (ANL), Argonne, IL (United States).

[2] Pil Jang, S., Choi, S.U. (2007). Effects of various parameters on nanofluid thermal conductivity. ASME Journal of Heat and Mass Transfer, 129(5): 617-623. https://doi.org/10.1115/1.2712475

[3] Meyer, J.P., Adio, S.A., Sharifpur, M., Nwosu, P.N. (2016). The viscosity of nanofluids: A review of the theoretical, empirical, and numerical models. Heat Transfer Engineering, 37(5): 387-421. https://doi.org/10.1080/01457632.2015.1057447

[4] Akbari, M., Galanis, N., Behzadmehr, A. (2011). Comparative analysis of single and two-phase models for CFD studies of nanofluid heat transfer. International Journal of Thermal Sciences, 50(8): 1343-1354. https://doi.org/10.1016/j.ijthermalsci.2011.03.008

[5] Wong, K.V., De Leon, O. (2010). Applications of nanofluids: Current and future. Advances in Mechanical Engineering, 2: 519659. https://doi.org/10.1155/2010/519659

[6] Siddappa, B., Abel, S. (1985). Non-Newtonian flow past a stretching plate. Zeitschrift für Angewandte Mathematik und Physik (ZAMP), 36(6): 890-892. https://doi.org/10.1007/BF00944900

[7] Khan, W.A. (2023). Significance of magnetized Williamson nanofluid flow for ferromagnetic nanoparticles. Waves in Random and Complex Media, 1-20. https://doi.org/10.1080/17455030.2023.2207390

[8] Khan, W.A. (2023). Dynamics of gyrotactic microorganisms for modified Eyring Powell nanofluid flow with bioconvection and nonlinear radiation aspects. Waves in Random and Complex Media, 1-11. https://doi.org/10.1080/17455030.2023.2168086

[9] Casson, N. (1959). Flow equation for pigment-oil suspensions of the printing ink-type. Rheology of Disperse Systems, 84-104.

[10] Dandapat, B.S., Holmedal, L.E., Andersson, H. I. (1998). On the stability of MHD flow of a viscoelastic fluid past a stretching sheet. Acta Mechanica, 130: 143-146. https://doi.org/10.1007/BF01187050

[11] Fang, T., Guo, F., Chia-fon, F.L. (2006). A note on the extended Blasius equation. Applied Mathematics Letters, 19(7): 613-617. https://doi.org/10.1016/j.aml.2005.08.010

[12] Mamaloukas, C., Spartalis, S., Manussaridis, Z. (2007). Similarity approach to the problem of second grade fluid flows over a stretching sheet. Applied Mathematical Sciences, 1(7): 327-338.

[13] Ali, B., Shafiq, A., Manan, A., Wakif, A., Hussain, S. (2022). Bioconvection: Significance of mixed convection and MHD on dynamics of Casson nanofluid in the stagnation point of rotating sphere via finite element simulation. Mathematics and Computers in Simulation, 194: 254-268. https://doi.org/10.1016/j.matcom.2021.11.019

[14] Alsallami, S.A., Zahir, H., Muhammad, T., Hayat, A.U., Khan, M.R., Ali, A. (2022). Numerical simulation of Marangoni Maxwell nanofluid flow with Arrhenius activation energy and entropy anatomization over a rotating disk. Waves in Random and Complex Media, 1-19. https://doi.org/10.1080/17455030.2022.2045385

[15] Ishak, A. (2011). MHD boundary layer flow due to an exponentially stretching sheet with radiation effect. Sains Malaysiana, 40(4): 391-395.

[16] Shahid, A., Huang, H.L., Khalique, C.M., Bhatti, M.M. (2021). Numerical analysis of activation energy on MHD nanofluid flow with exponential temperature-dependent viscosity past a porous plate. Journal of Thermal Analysis and Calorimetry, 143: 2585-2596. https://doi.org/10.1007/s10973-020-10295-9

[17] Pavlov, K.B. (1974). Magnetohydrodynamic flow of an incompressible viscous fluid caused by deformation of a plane surface. Magnitnaya Gidrodinamika, 4(1): 146-147. http://doi.org/10.22364/mhd

[18] Andersson, H.I. (1992). MHD flow of a viscoelastic fluid past a stretching surface. Acta Mechanica, 95(1): 227-230. http://doi.org/10.1007/bf01170814

[19] Khan, W.A., Ali, M., Shahzad, M., Sultan, F., Irfan, M., Asghar, Z. (2020). A note on activation energy and magnetic dipole aspects for cross nanofluid subjected to cylindrical surface. Applied Nanoscience, 10: 3235-3244. https://doi.org/10.1007/s13204-019-01220-0

[20] Khan, W.A., Waqas, M., Chammam, W., Asghar, Z., Nisar, U.A., Abbas, S.Z. (2020). Evaluating the characteristics of magnetic dipole for shear-thinning Williamson nanofluid with thermal radiation. Computer Methods and Programs in Biomedicine, 191: 105396. https://doi.org/10.1016/j.cmpb.2020.105396

[21] Seyedi, S.H., Saray, B.N., Chamkha, A.J. (2020). Heat and mass transfer investigation of MHD Eyring–Powell flow in a stretching channel with chemical reactions. Physica A: Statistical Mechanics and Its Applications, 544: 124109. https://doi.org/10.1016/j.physa.2019.124109

[22] Pinheiro, I.F., Serrano, H.L., Sphaier, L.A., Peixoto, F.C., Silva, V.N.H. (2019). Integral transform analysis of heat and mass diffusion in chemically reacting systems with Michaelis–Menten kinetics. International Communications in Heat and Mass Transfer, 100: 20-26. https://doi.org/10.1016/j.icheatmasstransfer.2018.10.003

[23] Crane, L.J. (1970). Flow past a stretching plate. Zeitschrift für angewandte Mathematik und Physik ZAMP, 21: 645-647.

[24] Cortell, R. (2006). Effects of viscous dissipation and work done by deformation on the MHD flow and heat transfer of a viscoelastic fluid over a stretching sheet. Physics Letters A, 357(4-5): 298-305. https://doi.org/10.1016/j.physleta.2006.04.051

[25] Bhattacharyya, K., Hayat, T., Alsaedi, A. (2013). Analytic solution for magnetohydrodynamic boundary layer flow of Casson fluid over a stretching/shrinking sheet with wall mass transfer. Chinese Physics B, 22(2): 024702. https://doi.org/10.1088/1674-1056/22/2/024702

[26] Mukhopadhyay, S. (2013). Casson fluid flow and heat transfer over a nonlinearly stretching surface. Chinese Physics B, 22(7): 074701. https://doi.org/10.1088/1674-1056/22/7/074701

[27] Rashidi, M.M.M., Pour, S.M. (2010). Analytic approximate solutions for unsteady boundary-layer flow and heat transfer due to a stretching sheet by homotopy analysis method. Nonlinear Analysis: Modelling and Control, 15(1): 83-95. https://doi.org/10.15388/NA.2010.15.1.14366

[28] Ali, B., Ahammad, N.A., Awan, A.U., Oke, A.S., Tag-ElDin, E.M., Shah, F.A., Majeed, S. (2022). The dynamics of water-based nanofluid subject to the nanoparticle’s radius with a significant magnetic field: The case of rotating micropolar fluid. Sustainability, 14(17): 10474. https://doi.org/10.3390/su141710474

[29] Fung, Y.C. (1984). Biodynamics: Circulation, Springer-Verlag. New York Inc.

[30] Mustafa, M., Hayat, T., Ioan, P., Hendi, A. (2012). Stagnation-point flow and heat transfer of a Casson fluid towards a stretching sheet. Zeitschrift für Naturforschung A, 67(1-2): 70-76. https://doi.org/10.5560/zna.2011-0057

[31] Shehzad, S.A., Hayat, T., Qasim, M., Asghar, S. (2013). Effects of mass transfer on MHD flow of Casson fluid with chemical reaction and suction. Brazilian Journal of Chemical Engineering, 30: 187-195. https://doi.org/10.1590/S0104-66322013000100020

[32] Naseer, M., Malik, M. Y., Nadeem, S., Rehman, A. (2014). The boundary layer flow of hyperbolic tangent fluid over a vertical exponentially stretching cylinder. Alexandria Engineering Journal, 53(3): 747-750. https://doi.org/10.1016/j.aej.2014.05.001

[33] Merkin, J.H., Najib, N., Bachok, N., Ishak, A., Pop, I. (2017). Stagnation-point flow and heat transfer over an exponentially stretching/shrinking cylinder. Journal of the Taiwan Institute of Chemical Engineers, 74: 65-72. https://doi.org/10.1016/j.jtice.2017.02.008

[34] Malik, M.Y., Naseer, M., Nadeem, S., Rehman, A. (2014). The boundary layer flow of Casson nanofluid over a vertical exponentially stretching cylinder. Applied Nanoscience, 4: 869-873.

[35] Sarojamma, G., Vendabai, K. (2015). Boundary layer flow of a Casson nanofluid past a vertical exponentially stretching cylinder in the presence of a transverse magnetic field with internal heat generation/absorption. International Journal of Mathematical and Computational Sciences, 9(1): 138-143.

[36] Mustafa, M., Khan, J.A., Hayat, T., Alsaedi, A. (2017). Buoyancy effects on the MHD nanofluid flow past a vertical surface with chemical reaction and activation energy. International Journal of Heat and Mass Transfer, 108: 1340-1346. https://doi.org/10.1016/j.ijheatmasstransfer.2017.01.029

[37] Awais, M., Raja, M.A.Z., Awan, S.E., Shoaib, M., Ali, H.M. (2021). Heat and mass transfer phenomenon for the dynamics of Casson fluid through porous medium over shrinking wall subject to Lorentz force and heat source/sink. Alexandria Engineering Journal, 60(1): 1355-1363. https://doi.org/10.1016/j.aej.2020.10.056

[38] Zhai, C., Wu, W. (2021). Heat and mass transfer performance comparison of various absorbers/desorbers towards compact and efficient absorption heat pumps. International Journal of Refrigeration, 127: 203-220. https://doi.org/10.1016/j.ijrefrig.2021.01.029

[39] Megahed, A.M., Abbas, W. (2022). Non-Newtonian Cross fluid flow through a porous medium with regard to the effect of chemical reaction and thermal stratification phenomenon. Case Studies in Thermal Engineering, 29: 101715. https://doi.org/10.1016/j.csite.2021.101715

[40] Barik, A.K., Mishra, S.K., Mishra, S.R., Pattnaik, P.K. (2020). Multiple slip effects on MHD nanofluid flow over an inclined, radiative, and chemically reacting stretching sheet by means of FDM. Heat Transfer—Asian Research, 49(1): 477-501. https://doi.org/10.1002/htj.21622

[41] Oyelakin, I.S., Mondal, S., Sibanda, P. (2016). Unsteady Casson nanofluid flow over a stretching sheet with thermal radiation, convective and slip boundary conditions. Alexandria Engineering Journal, 55(2): 1025-1035. https://doi.org/10.1016/j.aej.2016.03.003

[42] Ibrahim, W., Makinde, O.D. (2016). Magnetohydrodynamic stagnation point flow and heat transfer of Casson nanofluid past a stretching sheet with slip and convective boundary condition. Journal of Aerospace Engineering, 29(2): 04015037. https://doi.org/10.1061/(ASCE)AS.1943-5525.0000529

[43] Rudraswamy, N.G., Gireesha, B.J., Chamkha, A.J. (2015). Effects of magnetic field and chemical reaction on stagnation-point flow and heat transfer of a nanofluid over an inclined stretching sheet. Journal of Nanofluids, 4(2): 239-246. https://doi.org/10.1166/jon.2015.1143

[44] Gupta, S., Kumar, D., Singh, J. (2018). MHD mixed convective stagnation point flow and heat transfer of an incompressible nanofluid over an inclined stretching sheet with chemical reaction and radiation. International Journal of Heat and Mass Transfer, 118: 378-387. https://doi.org/10.1016/j.ijheatmasstransfer.2017.11.007

[45] Mini, G.S., Kumar, P.V., Shaik, M.I. (2024). Numerical simulations of chemically dissipative MHD mixed convective non-Newtonian nanofluid stagnation point flow over an inclined stretching sheet with thermal radiation effects. CFD Letters, 16(5): 37-58. https://doi.org/10.37934/cfdl.16.5.3758

NOMENCLATURE

a	Constant stretching rate
b	Free stream rate
$(c)_f$	Specific heat at constant pressure
u,v	Velocity components in x, y directions
U_w	Stretching velocity
U_∞	Free stream velocity
B_0	Strength of magnetic field
D_B	Brownian diffusion coefficient
D_T	Thermophoresis diffusion coefficient
V_w	Wall injection/suction velocity
γ	Chemical reaction parameter
ζ	Similarity variable
μ_B	Plastic dynamic viscosity
π	Product of component deformation
g	Gravitational acceleration
C	Concentration of the fluid
C_w	Concentration level of fluid at surface
C_∞	Ambient concentration
k_*	Absorption coefficient
κ	Thermal conductivity of fluid
$\hbar_f, \hbar_\theta$ and $\hbar_\phi$	Non-zero auxiliary parameters
χ_n	Characteristic function
D_i (i=1 to 7)	Arbitrary constants
N_f, N_θ and N_ϕ	Non-linear operators
L_f, L_θ and L_ϕ	Linear operators
M	Magnetic field parameter
Nt	Thermophoresis parameter
Nb	Brownian motion parameter
Pr	Prandtl number
Ω	Inclined sheet angle
σ_f	Electrical conductivity
ρ_p	Nanoparticles mass density
$(\rho c)_p$	Heat capacity of the nanoparticles
σ_*	Stefan -Boltzmann constant
ρ_f	Fluid density
$(\rho c)_f$	Fluid heat capacity
Gr	Local Grashof number due to temperature
Gc	Local Grashof number due to concentration
θ	Dimensionless temperature
ϕ	Dimensionless concentration
q_r	Radiative heat flux
A	Velocity ratio parameter
Gr_x	Temperature buoyancy parameter
Gc_x	Concentration buoyancy parameter
Q_0	Heat generation coefficient
Kr	Coefficient of chemical reaction
P_y	Yield stress
S	Suction parameter
Ge_x	Local Reynolds number
α	Thermal diffusivity of the fluid
β_c	Volumetric coefficient of mass expansion
β_T	Volumetric coefficient of thermal expansion
e_{ij}	(i,j)th component of the deformation

π_c	Critical value of the product based on non-Newtonian model
β	Casson parameter
R	Thermal radiation parameter
Le	Lewis parameter
T	Fluid temperature
T_w	Convective fluid temperature
T_∞	Ambient fluid temperature
q_w	Surface heat flux
q_m	Surface mass flux
τ_w	Surface shear stress
V_0	Initial strength of suction
C_{fx}	Coefficient of skin friction
Nu_x	Local Nusselt number
Sh_x	Local Sherwood number
f	Dimensionless stream function
f'	Dimensionless velocity
Sc	Schmidt number
Q	Heat source parameter
υ	Kinematic viscosity
ζ	Dimensionless variable
μ	Dynamic viscosity
$\tau = \frac{(\rho c)_p}{(\rho c)_f}$	Fraction of Heat Capability of Nanofluid to the Base Fluid
ψ	Stream function

Subscripts

f	Fluid
w	Wall
p	Nanoparticle
∞	Free stream